Journal of Materials Chemistry B

ROYAL SOCIETY OF CHEMISTRY

PAPER

View Article Online
View Journal | View Issue



Cite this: J. Mater. Chem. B, 2022, 10, 8419

# Hollow microneedle array fabrication using a rational design to prevent skin clogging in transdermal drug delivery†

Nur Unver,[a] Sedat Odabas,[bc] Gokcen Birlik Demirel [a] and O. Tolga Gul *[d]

Received 5th August 2022,
Accepted 27th September 2022

DOI: 10.1039/d2tb01648f

rsc.li/materials-b



Microneedle (MN) technology is promising to replace hypodermic needles for practical use and painless drug delivery. However, the complex top-down fabrication process of functional MN arrays is a bottleneck that hinders their widespread use. Here, we fabricate the tapered hollow MN array using a unique bi-level-tip by combining strain-engineering and capillary self-assembly of carbon nanotube (CNT) microstructures. Strain-engineering facilitated by the offset pattern of the catalyst enables the growth of bent, bi-level CNT microstructures while capillary self-assembly helps in constituting the tapered geometry of MNs. The bottom-up fabrication that consists of only two standard photolithography steps and CNT growth to form the scaffold of MNs followed by a polymer (polyimide) reinforcement step to impart mechanical stiffness to MNs provides scalable and fewer processing steps. The tapered shape of the MN allows an 8 times smaller force to pierce and penetrate the skin compared to the straight MN. The liquid delivery rate of the bi-level-tip MN is measured to be 26% better than the flat tip MN of the same lumen size as its geometry reduces skin clogging effect at the needle tip. In addition, cytotoxicity tests verify that the polyimide reinforced CNT-MNs are biocompatible for future *in vivo* applications.

## Introduction

The subcutaneous injection of drugs with hypodermic needles is a more effective method since the oral administration is not feasible due to poor drug absorption or enzymatic degradation in the gastrointestinal tract or liver.[1,2] However, the use of hypodermic needles requires special training for patients; otherwise they are limited to their clinical use. Pain and anxiety caused by hypodermic needles associated with their size in the patient are other concerns.[3,4] At this point, the subcutaneous injection with hypodermic needles is about to yield new generation drug delivery methods. Microneedles (MNs) appear to be excellent candidates for transdermal drug delivery due to their practical use in preventing accidental needle injuries, reduced size leading to improvements in mitigating patient complaints, and effective drug use enabling dose sparing.[5–15]

MNs with various types and functionalities have been fabricated by using various materials and fabrication techniques.[16–19] The feasibility and success of MN-mediated drug delivery largely depend on the functionality of MNs and the simplicity of their manufacture. Therefore, choosing an appropriate material which provides convenience and structural flexibility in fabrication is of great importance. For example, choosing silicon or metals as the building material of hollow MNs increases the number of processing steps in fabrication and the production time and cost.[20–22] In addition, the fabrication of MNs with the top-down approach limits the architecture compared to the bottom-up approach which is more scalable and flexible to build MNs. In this respect, carbon nanotubes (CNTs) emerge as an ideal material to form the scaffold of hollow MNs, considering the simplicity and flexibility of their synthesis. Catalyst patterning enables vertically aligned CNTs (VACNTs) to form architectures with arbitrary geometry.[23,24] Lyon *et al.* reported the successful fabrication of the CNT–MN array by creating the entire geometry of the MNs, including the lumen, with a single step of CNT synthesis.[25] The porous scaffold of VACNTs was then filled with polymer resin by spin coating to impart mechanical stiffness to CNT-MN. Although the reported work reduced process steps in MN fabrication by simple and flexible synthesis

[a] Department of Chemistry, Polatlı Faculty of Science and Letters, Ankara Hacı Bayram Veli University, Ankara, 06900, Turkey
[b] Biomaterials and Tissue Engineering Laboratory (BteLAB), Department of Chemistry, Faculty of Science, Ankara University, Ankara, 06560, Turkey
[c] Interdisciplinary Research Unit for Advanced Materials (INTRAM), Ankara University, Ankara, 06560, Turkey
[d] Department of Physics, Polatlı Faculty of Science and Letters, Ankara Hacı Bayram Veli University, Ankara, 06900, Turkey. E-mail: tolga.gul@hbv.edu.tr

† Electronic supplementary information (ESI) available. See DOI: https://doi.org/10.1039/d2tb01648f

of VACNTs, the MN geometry consists of a flat tip, straight hollow cylinder rather than the beveled tip or tapered geometry, which is mostly sought in hollow MNs in order to facilitate skin penetration and increase liquid flow rate to a medium.[26–28]

Fabricating scalable, non-planar or curved three-dimensional (3-D) microstructures is of great interest for advanced surfaces requiring applications.[29] But, it is considerably difficult to create identical structures in array using existing lithography techniques.[30–33] The microstructures formed by VACNT micropillars also tend to grow in a planar structure, if there are no manipulating mechanical factors to overcome the force holding the VACNT micropillars together in the population. However, there have been promising techniques that enabled the fabrication of non-planar or curved VACNT microstructures during or after the growth. De Volder *et al.* introduced strain-engineered growth of VACNTs by offset patterning of the catalyst that induces differential CNT growth rate between adjacent regions to form uniformly curved VACNT microstructures.[34] This allows creating a variety of bent VACNT microstructures during the growth depending on the geometry of the catalyst patterning. On the other hand, after the growth, capillary forces triggered by wetting or drying cause a shape deformation or rearrangement in VACNT microstructures called capillary self-assembly.[35–38] Capillary forces bring discrete VACNT micropillars into close contact while deforming VACNT microstructures such that curved or non-planar geometries can occur. Here, we present a novel approach to fabricate bi-level-tip, tapered hollow CNT-MN arrays by combining the strain-engineering during the growth and the capillary self-assembly with polyimide (PI) reinforcement after the growth. The resulting tapered geometry of the CNT-MN provides skin penetration with smaller insertion force while its bi-level-tip suppresses skin compression at the tip, enhancing the flow rate.

## Experimental

### Substrate preparation and CNT growth

4″ Si wafers with 500 μm thickness, (100) orientation and 300 nm thick oxide layer on top were used as substrates. Layers were patterned by successive lift-off processes and photolithographies. First, a 40 nm TiN layer was patterned by magnetron sputtering. Later, a 10 nm $Al_2O_3$ layer and 1 nm Fe as a catalyst layer were deposited by e-beam evaporation. After the lift-off process and cleaning, the wafer was diced into 1 cm × 1 cm pieces and saved for CNT growth and MN fabrication. CNT growth on catalyst patterned regions was performed in 1″ quartz tube furnace under atmospheric pressure. Catalysts were reduced with 50 sccm $H_2$ at varying temperatures (500, 600, 700, and 800 °C) for 5 min and then the furnace temperature was ramped up to the growth temperature (800 °C). CNT growth was triggered and maintained with a 10/40/10 sccm $C_2H_4/H_2/Ar$ gas combination. A 10 min growth is sufficient to achieve 250 μm tall CNT microstructures. After CNT growth, the furnace was cooled down to room temperature in the presence of 300 sccm Ar flow. CNT microstructures were observed by scanning electron microscopy (SEM).

### Polyimide reinforcement of CNT-MN array

We used poly(pyromellitic dianhydride-*co*-4,4′-oxydianiline), amic acid (PAA), as the reinforcement material. The substrate including CNT microstructures was inverted parallel to the PAA solution surface and slowly dipped into the PAA until it reached the tips of CNT microstructures. After PAA penetrated the base of CNT microstructures, the sample was retracted and then completely dipped into the PAA solution. After dipping, the substrate was reverted back with CNT microstructures up. The remaining PAA from CNT microstructures coated the silicon substrate and formed a base layer. For thermal curing, the substrate was placed on a preheated hotplate operating at 130 °C. Thermal curing at 130 °C was performed for 30 min and followed by additional curing at 150 °C and 200 °C for 30 min each. The substrate was then placed into an oven at 250 °C for 2 h. With thermal curing, the imidization of PAA forms PI. After thermal curing, PI reinforced CNT microstructures (PICNT-MN array) were separated from silicon substrate by a razor blade.

### Liquid reservoir fabrication and PICNT-MN array attachment

The nonflexible liquid reservoir was fabricated by a 3D-printer using a polylactic acid (PLA) filament with dimensions of 1.2 cm × 1.2 cm × 0.4 cm. PICNT-MN array was attached to the bottom of the nonflexible liquid reservoir with epoxy adhesive. The assembly was placed into an oven at 50 °C for 4 h to promote the adhesion. The flexible liquid reservoir was fabricated from polydimethylsiloxane (PDMS). A Sylgard 184 silicon elastomer and curing agent were mixed in a ratio of 10 : 1 and placed in a vacuum chamber to eliminate air bubbles. The mixture then was poured on glass molds which were designed to form top and bottom parts of the flexible liquid reservoir. Curing was carried out at 80 °C for 1 h. After PDMS peeling off, the top and bottom PDMS parts were bonded together with oxygen plasma treatment. For the attachment of PICNT-MN array to the flexible liquid reservoir, PDMS resin as an adhesive was used and cured at 80 °C for 30 min.

### Mechanical stability and liquid delivery of the PICNT-MN array

The mechanical stability of the PICNT-MN under axial and transverse load forces was tested by a micromechanical testing machine. The PICNT-MN array was mounted on the lower station while a conical stainless mill with 1 $mm^2$ cross-sectional area was mounted on the upper station of the testing machine. Load force *versus* displacement was measured by pressing the mill on PICNT MN.

In liquid delivery experiments through the PICNT-MN array, deionized (DI) water and methylene blue solution were used as liquids. 1% agarose hydrogel and rat skin (*in vitro*) were selected as delivery media. No animals were sacrificed for this work. Rat skins were collected from the already sacrificed animals in other experiments. Rat skin samples were shaved and cleaned prior to use. A syringe attached nonflexible liquid reservoir and a syringe pump were used to measure liquid delivery performance of the PICNT-MN array. Liquid flow rates

 

through the PICNT-MN array during delivery to air (no medium), hydrogel and the skin were measured.

### Skin penetration and cytotoxicity tests of PICNT-MN array

In order to evaluate the PICNT-MN penetration, a standard hematoxylin and eosin (H&E) staining was performed for general histological assessment prior to depth penetration test. Briefly, rat skin tissues were first fixed with 10% natural formalin, dehydrated in gradual ethanol and washed in xylene. Then samples were immersed in paraffin wax at 55 °C. 10 μm-thick serial sections were obtained from paraffin blocks and sections were mounted on a glass slide prior to staining. Imaging was performed by using a semi-automated light microscope.

The biocompatibility of the samples in terms of their possible cytotoxicity were evaluated by indirect MTT assay. Briefly, L929 mouse fibroblast cells were seeded on a 96 well plate at a density of $1 \times 10^4$ cells well$^{-1}$ and cultured with DMEM F/12 supplemented with 10% FBS, 1% antibiotic/antimycotic solution, 1% L-glutamine, at 37 °C and 5% $CO_2$. Samples were UV-sterilized for 30 min prior to use and incubated with culture media for about 24 h for the elution test. Later on, cells were incubated with that elution media and possible cytotoxicity of the samples were evaluated up to 48 h compared to tissue culture polystyrene plate (TCPS). In addition to the MTT assay, a live/dead staining (calcein/EtBr) was also performed to the cells cultured with elution media for 24 h. For the staining, cells were observed under a fluorescence microscope with an FITC standard filter set.

## Results and discussion

The horizontal geometry of CNT microstructures is determined by catalyst patterning while the vertical geometry is shaped with CNT growth and post-growth processing. Fig. 1 depicts the TiN underlayer and the catalyst ($Fe/Al_2O_3$) layer patterning on $SiO_2$ with two successive photolithography, deposition and lift-off steps. The first photolithography is applied through the photomask 1 to create a hollow circular pattern on a photoresist film. With the following 40 nm TiN deposition and lift-off process, a hollow circular TiN underlayer is formed on $SiO_2$. For the second photolithography, the photomask 2 is designed to have the same hollow circular pattern used in the photomask 1 and additional four trapezoids that are adjacent to the hollow circular pattern. The continuous catalyst layer ($Fe/Al_2O_3$ 1/10 nm) is patterned

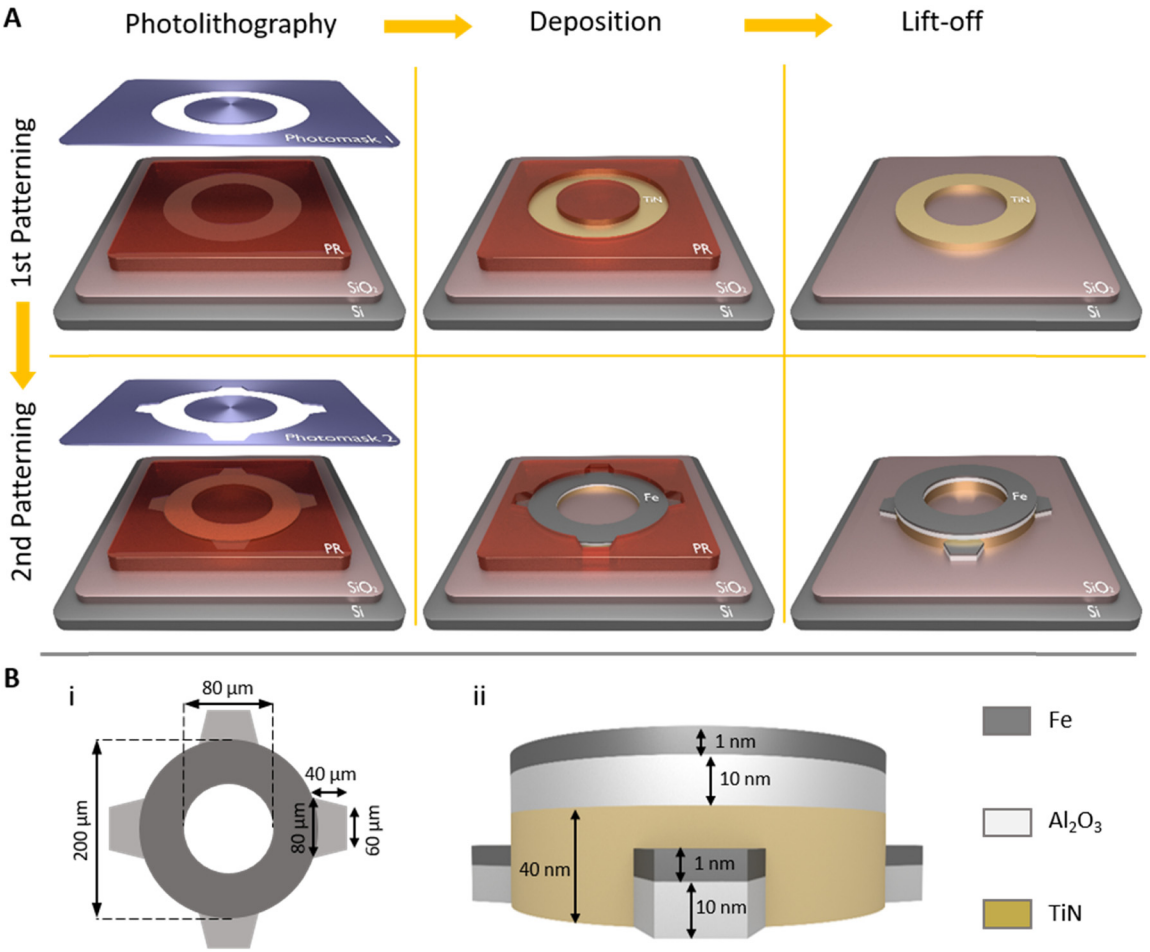


Fig. 1 (A) Illustration of catalyst patterning with two successive photolithography, deposition and lift-off steps. (B) (i) The horizontal and (ii) the vertical views of the pattern with size values.

partly on the TiN deposited hollow circle and partly on $SiO_2$ in trapezoid shapes. Therefore, the hollow circle consists of a TiN underlayer (on $SiO_2$) and the catalyst layer while trapezoid shaped regions around the hollow circle consist only of the catalyst layer (on $SiO_2$). The hollow circle is patterned with 200 μm outer diameter and 80 μm inner diameter. The trapezoid shapes have the geometry, bases of 60 μm and 80 μm and the height of 40 μm (Fig. 1(B)).

Vertical CNT growth on the patterned catalyst provides the formation of 3-D CNT microstructures that are shaped according to the pattern. CNT micropillars grew on the hollow circular pattern forms the hollow CNT microcylinder which will consist of the scaffold of the hollow microneedle while CNT micropillars grew on trapezoid patterns build the CNT microcolumns whose role will be discussed in detail later (Fig. 2(A)–(C)). The average CNT growth rates from the catalyst patterned on $SiO_2$ and on 40 nm TiN underlayer are 25 μm $min^{-1}$ and 20 μm $min^{-1}$, respectively. The catalyst and underlayer interaction is a key factor in the CNT growth rate.[39–41] De Volder *et al.* reported that the thickness of TiN underlayer is also a determining factor on CNT growth rate.[34] These different growth rates caused by different underlayers induce relatively long and short CNT micropillar array

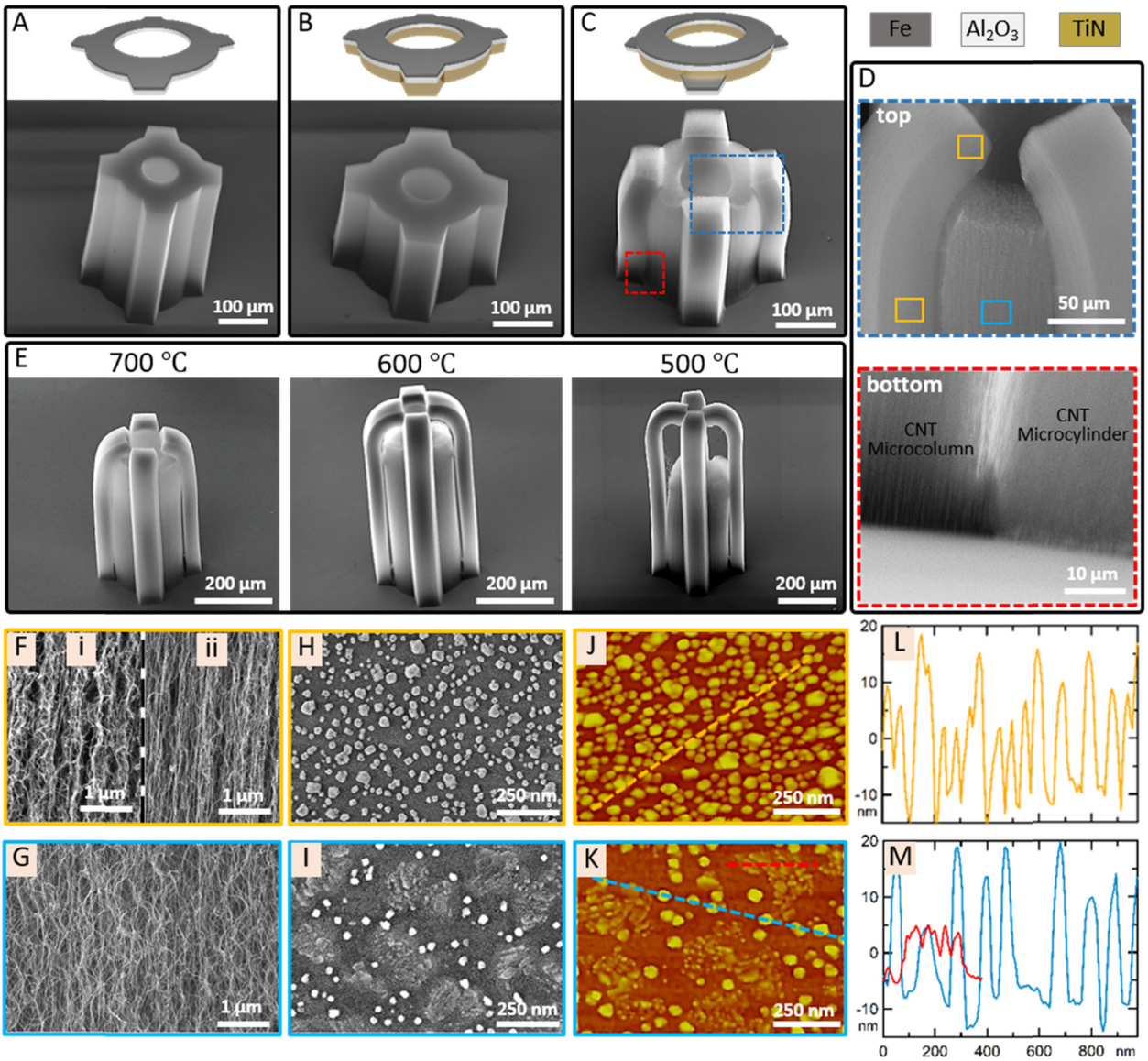


Fig. 2 CNT microstructures grew on the catalyst that (A) entirely patterned on $SiO_2$ without TiN, (B) entirely patterned on TiN underlayer on $SiO_2$, (C) continuously patterned partly on TiN (hollow circular pattern) and partly on $SiO_2$ (trapezoid patterns). (D) The magnified views of the top and the bottom portions of the CNT microstructure in (C). (E) CNT microstructures, grew on catalysts reduced at different temperatures (700, 600 and 500 °C), with different growth rates. The magnified SEM images of CNT micropillars at (F) (i) the top and (ii) lower regions of the microcolumns and (G) the microcylinder. SEM images of the catalyst (H) on $SiO_2$ and (I) on TiN underlayer on $SiO_2$. AFM images of the catalyst (J) on $SiO_2$ and (K) on TiN underlayer on $SiO_2$, showing morphological difference. (L and M) AFM height profiles of the dashed lines in (J) and (K). The red AFM profile in (M) represents the height distribution of the TiN island (the red dashed line in (K)) formed after the reduction in $H_2$.

 

growth. For example, when the catalyst is entirely patterned on $SiO_2$ without TiN underlayer deposition (first photolithography is skipped), the CNT microstructure grows up to 250 μm in length in 10 min (Fig. 2(A)). On the other hand, if the catalyst is continuously patterned on the TiN underlayer so that it covers the entire pattern including trapezoids around the hollow circle (first photolithography is skipped, and the TiN underlayer is also deposited after the second photolithography), the CNT microstructure reaches to 200 μm length in the same time span (Fig. 2(B)). Moreover, when the continuous catalyst is patterned on different adjacent underlayers, as seen in Fig. 2(C), the CNT microstructure can be formed in curved geometries as a result of the strain-engineered growth.[34] The hollow CNT microcylinder (grown from the catalyst on the TiN underlayer) bends the CNT microcolumns (grown from the catalyst on the $SiO_2$ underlayer) towards itself. The bending mechanism is the effect of the stress induced by different growth rates of CNT micropillars at the boundary of two different adjacent underlayers. The stress between CNT micropillars is governed and maintained through van der Waals interactions and the entanglement of CNTs at the boundary region.[34]

For further investigation of the strain-engineered growth of the CNT microstructure, we focused on the boundary region of the CNT microstructure. The top portions of the CNT microcolumns slightly curve over and separates from the hollow CNT microcylinder (Fig. 2(D)). The separation of neighboring CNT arrays from each other at the boundary of differentially grown regions is also visible in the SEM image of the bottom portion of the CNT microstructure (Fig. 2(D)). The degree of entanglement and the strength of van der Waals interactions are determinants for holding the whole structure together. If the determinants cannot compete with shear stress between two regions, then the separation is inevitable. The magnitude of shear stress is strictly correlated with the growth rate difference between the neighboring CNT arrays. In the present case, the growth rate difference between CNT arrays on the TiN underlayer and on $SiO_2$ underlayer is 5 μm $min^{-1}$, which is enough to predominate the determinants for the separation. The separation of the CNT microcolumns from the hollow CNT microcylinder due to the growth rate difference resulted in the formation of the CNT microstructure with a bi-level apex.

Since the strain-engineering needs contact of the neighboring CNT arrays in order to perform bending, it requires the bending to occur before the separation. We have investigated the early stage of the CNT microstructure growth and its evolution with time (Fig. S1, ESI†). Bending of CNT microcolumns starts at the very beginning of the growth phase and evolves with continuing growth until the separation. The curvature in the bent portion of the CNT microcolumns is determined by the growth rate difference between the neighboring CNT arrays. As the growth rate difference increases, the curvature induced by the strain-engineering increases and the separation occurs earlier. We have successfully controlled the curvature of the CNT microcolumns by controlling the growth rate difference by reducing the catalyst with $H_2$ at different temperatures before the growth phase. Recently, we have reported that catalyst reduction temperature prior to CNT growth is a critical parameter for shaping the catalyst morphology which later greatly effects CNT growth rate.[42–44] Catalyst reduction at lower temperature induces a more uniform and denser catalyst formation than at higher temperature, resulting with enhanced growth rate. Therefore, applying the same strategy here enables to control the growth rate difference between the CNT microcolumns and the hollow CNT microcylinder. The average CNT growth rate differences were found 5, 7, 10 and 20 μm $min^{-1}$ for catalysts reduced at 800, 700, 600 and 500 °C, respectively. SEM images in Fig. 2(E) show three CNT microstructures grown after catalyst reductions at three different temperatures (700, 600, and 500 °C). Note that the CNT microstructure in Fig. 2(C) corresponds to the case in which catalysts are reduced at 800 °C. As hypothesized, the CNT microcolumns grow longer than the hollow CNT microcylinder and bend more sharply with decreasing catalyst reduction temperature.

We have also investigated morphological differences of CNTs and catalysts on $SiO_2$ and TiN underlayers. The CNTs in the microcolumns show two different morphologies depending on their location. At the top region of the microcolumns, corresponding to the bent portion, CNTs are less aligned presumably due to the force that withstands the fast growing CNTs by the slow growing CNTs in the hollow microcylinder (Fig. 2(F)-i). The CNTs at the lower region of the microcolumns are those that grow after the separation so these CNTs are more aligned since there is no force opposing their motions (Fig. 2(F)-ii). On the other hand, the CNTs of the hollow microcylinder are sparse and poorly aligned compared to the CNTs of the microcolumns (Fig. 2(G)). Their poor alignment may be attributed to their slow growth rate but their sparse morphology needs a detailed investigation in terms of the catalyst morphology. Fig. 2(H)–(K) show SEM and atomic force microscopy (AFM) images of catalysts formed on $SiO_2$ and TiN underlayers after reduction in $H_2$/Ar at 800 °C. Smaller and larger catalysts with average heights of 10 nm and 30 nm form on $SiO_2$, respectively. The catalyst density nevertheless affirms denser CNT growth in the microcolumns regardless of the catalyst size. Bimodality in the catalyst size is the result of catalyst coarsening and diffusion at high temperature reduction that we have recently reported with its consequences on CNT morphology.[43] Moreover, the reduction induces TiN island formation of less than 10 nm high and hundreds of nanometers wide besides catalysts that are 20–30 nm high on average. The catalysts are localized as inhomogeneously distributed clusters in the regions bounded by TiN islands, resulting in a larger spacing between catalyst clusters. Less dense catalyst formation on TiN than on $SiO_2$ explains the sparse CNT morphology in the hollow microcylinder.

Individual CNTs are extremely strong materials compared to other 1-D nanomaterials.[45–47] 3-D CNT microstructures tend to buckle when encountering a small resistance due to the high-aspect ratio of and interspacing between CNT micropillars. The high porosity of CNT microstructure limits their use without reinforcement in contact required applications including biomedical applications. Therefore, their reinforcement with a resin to gain mechanical stiffness prior to their practical use is necessary.[48]

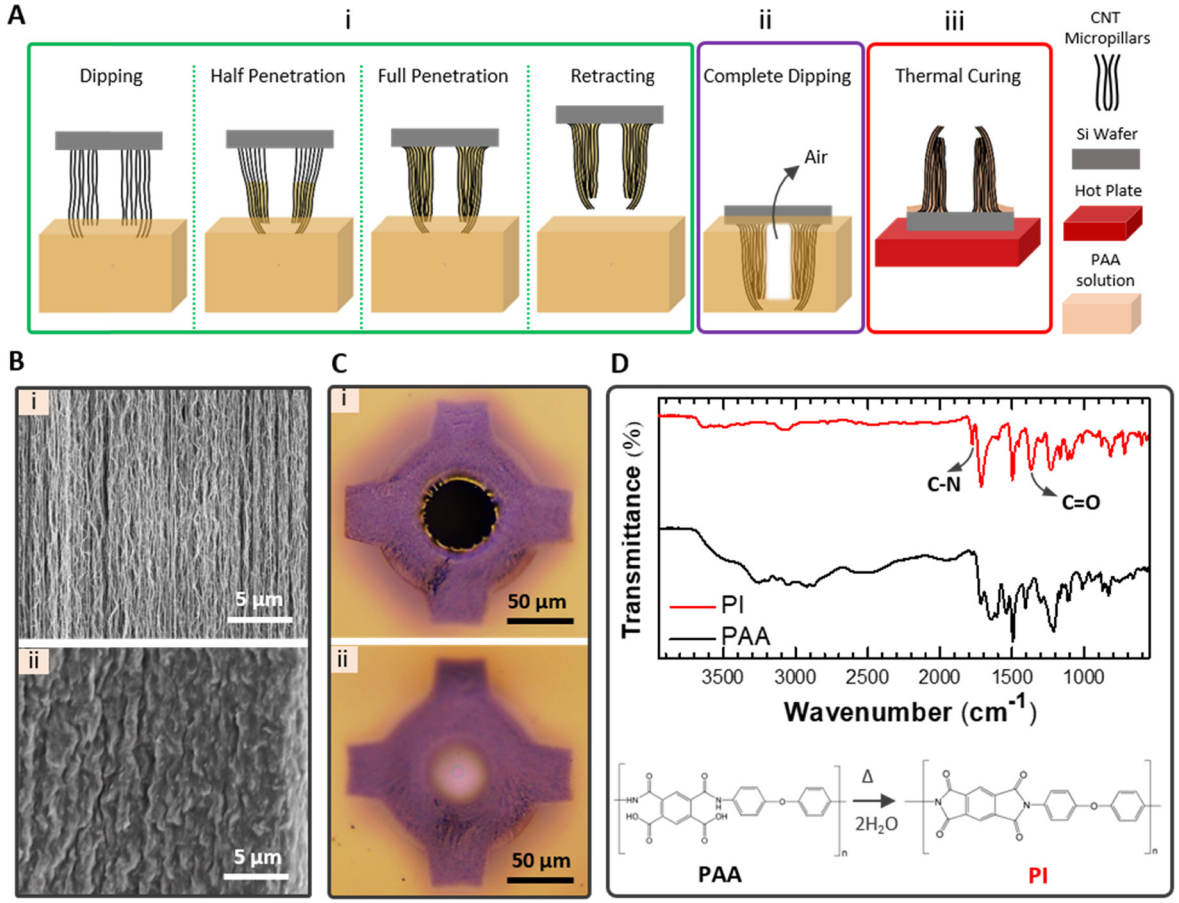


Fig. 3 (A) Illustration of the PI reinforcement process of CNT-MN. (B) Magnified SEM images of the CNT microstructure (i) before (porous) and (ii) after (non-porous) PI reinforcement. (C) Bottom views of PI reinforced CNT-MNs with (i) dipping method (PI-free lumen) and (ii) spin coating method (blocked lumen with PI layer). (D) FT-IR spectrums of PAA and PI after thermal curing at 250 °C.

Fig. 3(A) depicts the reinforcement process of the CNT microstructures by PAA solution which will be converted to PI after thermal imidization. The reinforcement process includes three key steps: (i) the inverted sample is lowered until the tips of CNT microstructures touch the PAA solution and after waiting for the PAA solution to drive into the CNT micropillar spacing, and then it is retracted, (ii) the sample is quickly dipped into the PAA solution until it reaches the $SiO_2$ surface and then is removed, and (iii) the sample is reverted back and rapidly transported on a preheated hot plate (130 °C) for thermal curing.

The first step enables tip-to-base PAA penetration of each CNT microstructure along CNT micropillars by capillary action while leaving the lumen empty. With the capillary action of PAA, porous CNT microstructures transform into non-porous CNT microstructures (Fig. 3(B)). PAA forms π–π interaction and hydrogen bonds through its aromatic backbone and hydroxyl and carboxyl groups of CNTs.[25,49] Dipping the sample completely into the PAA solution in the second step helps creating a base layer under the CNT microstructures. During the complete dipping, PAA filling of the lumen is prevented by the air entrapped in the lumen of the non-porous CNT microstructure. Lyon *et al.* reported that drop casting polymer over the sample and following spin coating create clear lumens.[25] We found that filling the interspacing of CNT micropillars with PAA by dipping method is more controllable rather than by drop casting over the sample to form the PAA-free lumen otherwise sometimes a thin layer, which blocks liquid flow later, is formed at the base of the lumen using the drop casting method (Fig. 3(C)). The third step allows the thermal imidization to form PI. The evaporation of solvent molecules and the imidization are two subsequent stages obtained with gradual temperature increment.[50] We observed that a rapid solvent evaporation is favorable in order to limit PAA mobility that may cause the lumen filling. Thus, the rapid transfer of the sample on a preheated hot plate after the dipping process was found highly beneficial for accelerating PAA immobility. The imidization of PI is ensured by Fourier transform infrared spectroscopy (FT-IR). The intensity peaks at 1370 $cm^{-1}$ and 1780 $cm^{-1}$, corresponding to C–N and C=O stretching vibrations of imide, appear after thermal curing at 250 °C while the FT-IR spectrum of PAA does not have these peaks (Fig. 3(D)).[50,51] Hereafter, we denote PICNT-MNs to refer PI reinforced CNT-MNs which correspond to CNT microstructures after PI reinforcement.

The CNT microstructures, formed by both the strain-engineering and ordinary growth, were mechanically strengthened with PI reinforcement. SEM images of the strain-engineered

 

and ordinarily grown CNT microstructures before capillary self-assembly are given in Fig. 4(A). The capillary self-assembly that occurs during both PI penetration and the solvent evaporation induces different shape transformations in the strain-engineered and ordinarily grown CNT microstructures due to variations in their structures. Lateral and axial forces exerted on CNT microstructures during the capillary self-assembly are involved in shaping PICNT-MNs (Fig. 4(B)). The hollow CNT microcylinder contracts toward the axis of the cylinder under the action of the lateral forces.[36] The axial forces, on the other hand, create a stress that pulls it downward especially at the base of the CNT microcylinder.[36] As a result, the combination of these two forces creates a contracted hollow microcylinder with a slope toward the apex. The CNT microcolumns on the sides of the hollow CNT microcylinder also experience the same forces and take shape accordingly as they are in contact with the hollow CNT microcylinder through PAA solution and shape. The strain-engineered growth of the CNT microstructure has a critical role on creating

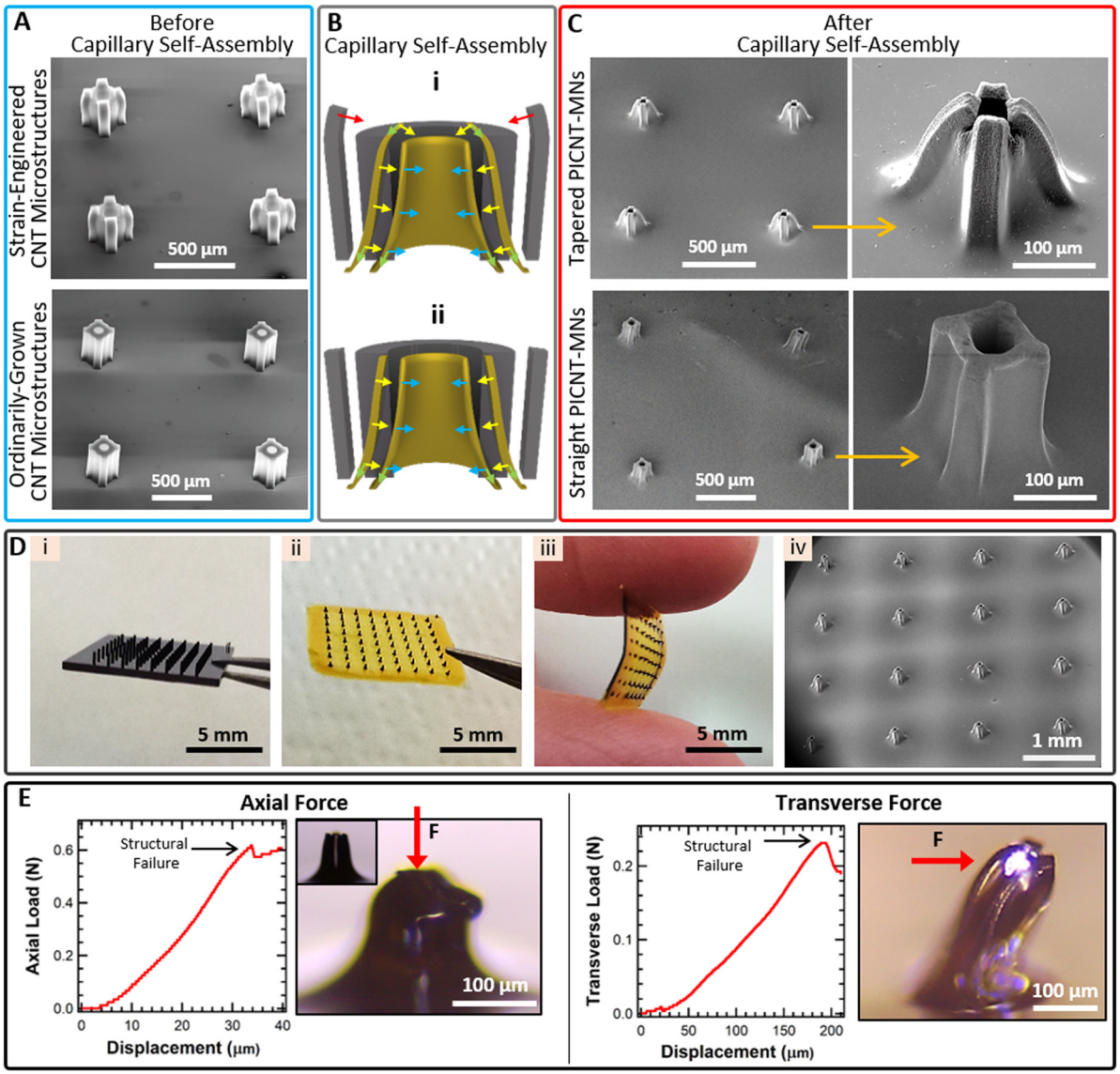


Fig. 4 (A) SEM images of the strain-engineered and ordinarily grown CNT microstructures before capillary self-assembly. (B) Schematics depicting shape transformations of (i) the strain-engineered and (ii) ordinarily grown CNT microstructures during capillary self-assembly. Gray models on the back represent the CNT microstructures before capillary self-assembly while yellowish models on front represent PICNT-MNs formed with capillary self-assembly. Arrows represent lateral forces exerted on hollow CNT microcylinders (blue) and CNT microcolumns (yellow), axial forces on the hollow CNT microcylinders and the CNT microcolumns (green). Red arrows indicate bending of the CNT microcolumns on the hollow CNT microcylinder due to the strain-engineered growth. (C) SEM images of the tapered and the straight PICNT-MNs formed after capillary self-assembly. (D) Images of (i) CNT microstructures on $SiO_2$ before PI reinforcement, (ii) and (iii) PICNT-MN array after PI reinforcement and peel off from $SiO_2$, (iv) 4 × 4 PICNT-MN array after PI reinforcement under SEM. (E) Axial and transverse forces *versus* displacement curves of the tapered PICNT-MN. Optical microscope images of the tapered PICNT-MNs after forces were applied. The inset in the first image is the optical microscope image of the tapered PICNT-MN before axial force was applied.

tapered PICNT-MNs when coupled with capillary self-assembly. The tips of the CNT microcolumns that previously bent towards CNT microcylinder due to strain-engineered growth are bent further by the resultant of lateral and axial forces during capillary self-assembly, creating a tapered geometry (Fig. 4(C)). However, for ordinarily grown CNT microstructures, the capillary self-assembly alone is not sufficient to create a tapered geometry for PICNT-MNs although it induces a shrinkage towards the cylinder axis in the structure (Fig. 4(C)).

Thus, these results confirm the critical role of the strain-engineered growth to create bi-level, tapered PICNT-MNs. PICNT-MNs, created as a result of the strain-engineered growth and the capillary self-assembly, were termed the tapered PICNT-MNs while PICNT-MNs, created as a result of ordinary growth and the capillary self-assembly, were termed the straight PICNT-MNs for simplicity. The shape transformation caused 67% and 48% reduction in the tip area of the tapered and the straight PICNT-MNs, respectively. The outer tip diameters of the tapered and the straight PICNT-MNs (measured from one micro-column to the opposite) were about 70 ± 5 μm and 145 ± 7 μm, respectively. The lumens of both PICNT-MNs were calculated as 50 ± 5 μm. Original heights (250 μm) of both PICNT-MNs were shortened 20% due to the 50 μm thick PI base formation at the bottom after the PI reinforcement. After thermal curing of PAA, the PI base is easily peeled from the Si wafer by a razor blade. The PI base thickness, measured to be 50 μm, is mechanically durable for separation from the Si wafer without tearing and also flexible for applying to uneven surfaces. We have fabricated PICNT-MN arrays consisting of 4 × 4, 5 × 5, 6 × 6 and 8 × 8 MN configurations in which MNs were designed to be 1 mm apart on the PI base of 1 cm × 1 cm total area. In the SEM image of the 4 × 4 PICNT-MN array, it is clearly seen that PICNT-MNs have uniform size and morphology, including their bi-level, tapered tips (Fig. 4(D)).

Higher CNT microstructures can be grown in order to fabricate taller PICNT-MNs by changing the CNT growth parameters such as extending growth duration or lowering the catalyst reduction temperature. However, the present size of the PICNT-MN is adjusted to penetrate the skin and prevent the stimulation or at least minimal stimulation of pain receptors.

The mechanical stability of the tapered PICNT-MN was measured before the penetration. Measurements were performed by applying axial and transverse forces on the PICNT-MN with a conical stainless mill which has a 1 $mm^2$ cross-sectional tip area. With the advantage of low cross-sectional tip area of the stainless mill, resistance of the single PICNT-MN to the applied force was measured as a function of displacement that corresponds to structural deformation in the tapered PICNT-MN (Fig. 4(E)). Both the axial and transverse forces suddenly dropped after linear increases. The linear increases in the loading force *versus* displacement curves before the sudden drops indicate elastic deformation in the tapered PICNT-MN. The sudden drop in the force points to a structural failure in the tapered PICNT-MN. Therefore, the maximum applied force to the tapered PICNT-MN is required to be lower than the threshold. The minimum axial and transverse forces that cause the structural failure of the single PICNT-MN, which has the aforementioned geometrical properties, were measured to be 0.62 N and 0.23 N, respectively.

Two types of liquid reservoirs, nonflexible and flexible, made out of PLA and PDMS were fabricated. The nonflexible liquid

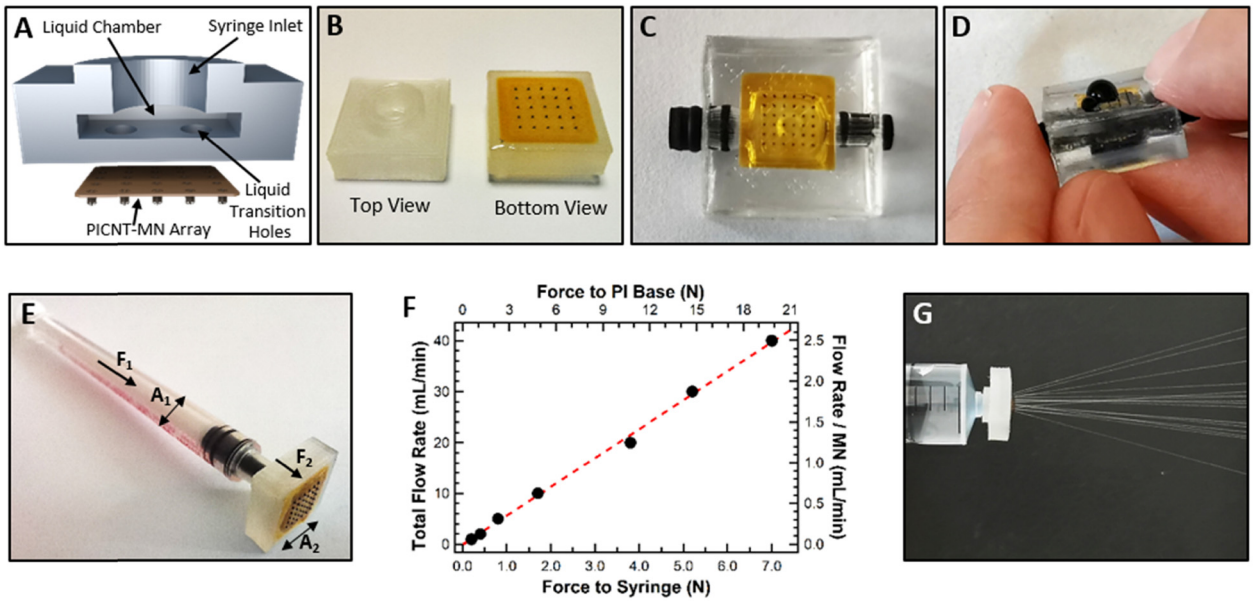


Fig. 5 (A) The schematic of the nonflexible liquid reservoir cut in the middle for detailed view. (B) Top and bottom view of the PICNT-MN array attached nonflexible liquid reservoir. (C) The view of the PICNT-MN array attached flexible liquid reservoir. (D) Ejection of methylene blue solution from the PICNT-MN array by applying a small pressure to the flexible liquid reservoir with a finger. (E) A syringe inserted nonflexible liquid reservoir ready for liquid delivery operation with the PICNT-MN array attachment. (F) Force (applied on the syringe and the PI base) *versus* flow rate (total flow rate from 16 MNs and flow rate per MN). The red dashed line is the linear fit to experimental data points. (G) Ejection of DI water from 4 × 4 PICNT-MN array with 2.5 mL $min^{-1}$ flow rate per MN.

 

reservoir was fabricated by a 3D-printer using PLA filament with dimensions of 1.2 cm × 1.2 cm × 0.4 cm. All parts including four small holes at the bottom for liquid transition to the PICNT-MN array, one large hole at the top for a syringe connection and a liquid chamber were fabricated during the printing without requiring an additional drilling later (Fig. 5(A)). The PICNT-MN array was adhered to the bottom of the nonflexible liquid reservoir with epoxy adhesive from the edges of the PI base, leaving MN array region adhesive-free so that the liquid transition from the holes of the nonflexible liquid reservoir to the PICNT-MN array are not blocked by the epoxy adhesive (Fig. 5(B)). A syringe was inserted into the hole at the top of the nonflexible liquid reservoir to maintain liquid delivery experiments (Fig. 5(E)).

The nonflexible liquid reservoir is highly functional for liquid delivery measurements since it can be used in a syringe pump after a syringe attachment. On the other hand, the flexible liquid reservoir was fabricated for practical skin applications. PDMS based flexible liquid reservoir has dimensions of 2 cm × 2 cm × 0.6 cm. It has two side holes on two opposite sides for liquid filling and one hole at the bottom for liquid transition to the PICNT-MN array. The PICNT-MN array was attached to the bottom of the flexible liquid reservoir with PDMS resin and the side holes were closed with stopples after liquid filling (Fig. 5(C)).

The first liquid delivery test of the PICNT-MN array was performed as a liquid flow into the air without application to a target. Methylene blue solution flow through the PICNT-MN array attached to the flexible liquid reservoir was carried by pressing on the top of the reservoir with a small force. Fig. 5(D) shows the methylene blue solution ejection of some MNs due to the small applied force (Movie S1, ESI†). However, it was observed that all MNs were able to deliver the solution without tearing of the PI base when the reservoir was pressed with sufficient force. For more quantitative investigation on the liquid delivery performance of the PICNT-MN array, the nonflexible liquid reservoir mounted on a syringe was loaded onto a syringe pump equipped with a digital force meter. We aimed to measure the force exerted by the syringe pump on the syringe while operating at a set liquid flow rate. This allows simultaneous measurement of the liquid flow rate through the PICNT-MN array and the resulting applied force. Moreover, we calculated the force exerted by the liquid on the PI base as a result of the thrust of the syringe pump in order to determine the force that the PI base can tolerate without being damaged. For example, for 4 × 4 PICNT-MN array; when liquid flow rate was set to 40 mL $min^{-1}$, the force exerted by the syringe pump was measured 7 N ($F_1$) on the syringe whose interior cross sectional area ($A_1$) is of $1.73 \times 10^{-5}$ $m^2$ (1 cc syringe with 4.7 mm inner diameter). The force ($F_2$) exerted by the liquid on the PI base, which has the surface area ($A_2$) of $4.90 \times 10^{-5}$ $m^2$ exposed to the liquid pressure after adhesion to the nonflexible liquid reservoir, is calculated as 19.8 N by Pascal law. Fig. 5(F) gives the force values exerted on the syringe and the PI base with varying liquid flow rates. The linear relationship between the applied force and the liquid flow rate is an expected result as long as no damage occurs on the PICNT-MN array or the PI base. The liquid flow rate per MN up to 2.5 mL $min^{-1}$ is successfully tested for water delivery to the air (Fig. 5(G) and Movie S2, ESI†). The repeated tests at this flow rate (>100 tests with 1 cc syringe fully filled with water) did not cause any damage to either the PICNT-MN array or the PI base. But the repeated liquid flow tests at higher rates (>3.0 mL $min^{-1}$ per MN after 12 tests with 1 cc syringe fully filled with water) caused the PI base to tear from the adhesion region due to excessive liquid pressure (Fig. S2, ESI†). Even though it tore from the adhesion region when the flow rate exceeded 3.0 mL $min^{-1}$ per MN which approximately corresponds to 23.8 N force exerted, there was no damage observed on the PI base. In liquid delivery to air, we found that the tapered and the straight PICNT-MNs showed similar performance as both PICNT-MNs had the same lumen size and there was no medium that clogged tips of MNs.

Prior to the liquid delivery measurements on a medium, the minimum applied force required for the PICNT-MN arrays to pierce and penetrate into the rat skin (*in vitro*) were determined. Fig. 6(A) shows the force per MN *versus* displacement curve that is measured with a digital force meter during the successful insertion of the tapered PICNT-MN array into the skin. We measured the minimum force to pierce the skin per MN to be about 0.15 N, corresponding to the point where the curve changes from parabolic to linear increasing trend. The optical microscope image confirmed that the piercing occurred at this force value (Fig. S3, ESI†). The force required for a MN insertion into the human skin as a function of MN's interfacial area was modeled based on experimental data by Davis *et al.*[28] Accordingly, the insertion force per MN, considering the geometry of the tapered PICNT-MN, is approximately calculated to be about 0.03–0.18 N, which is consistent with our experimental force values. After the piercing, the skin penetration process begins, corresponding to the linearly increasing area in the curve.

The linear increase of the force during the penetration is attributed to the conical geometry of the tapered PICNT-MN that requires increasing force due to its increasing penetrated area with continuing insertion. The insertion was terminated after the sufficient penetration depth was achieved. In addition, the insertion force per MN was measured for the straight PICNT-MN for comparison. The force *versus* displacement curves for both PICNT-MNs are given as the inset in Fig. 6(A). The minimum force to pierce the skin per the straight PICNT-MN was approximately 1.3 N, which is more than 8 times the force required for the tapered PICNT-MN. The characteristic difference between the two curves was attributed to the different geometries of the tapered and straight PICNT-MNs. Histological assessment which is depicted in Fig. 6(B) indicates that the PICNT-MN could penetrate the skin without bleeding or tissue disintegration. The collective results show the effectiveness of the PICNT-MNs. Besides, these skin insertions show apparent correlation with the recent literature.[52,53] The tapered PICNT-MN array was viewed in SEM after repeated skin insertions and cleaning with ethanol and DI water (Fig. 6(C)). The PICNT-MNs appear to show no signs of structural deformation when compared to the SEM image taken before the penetration in Fig. 4(C).

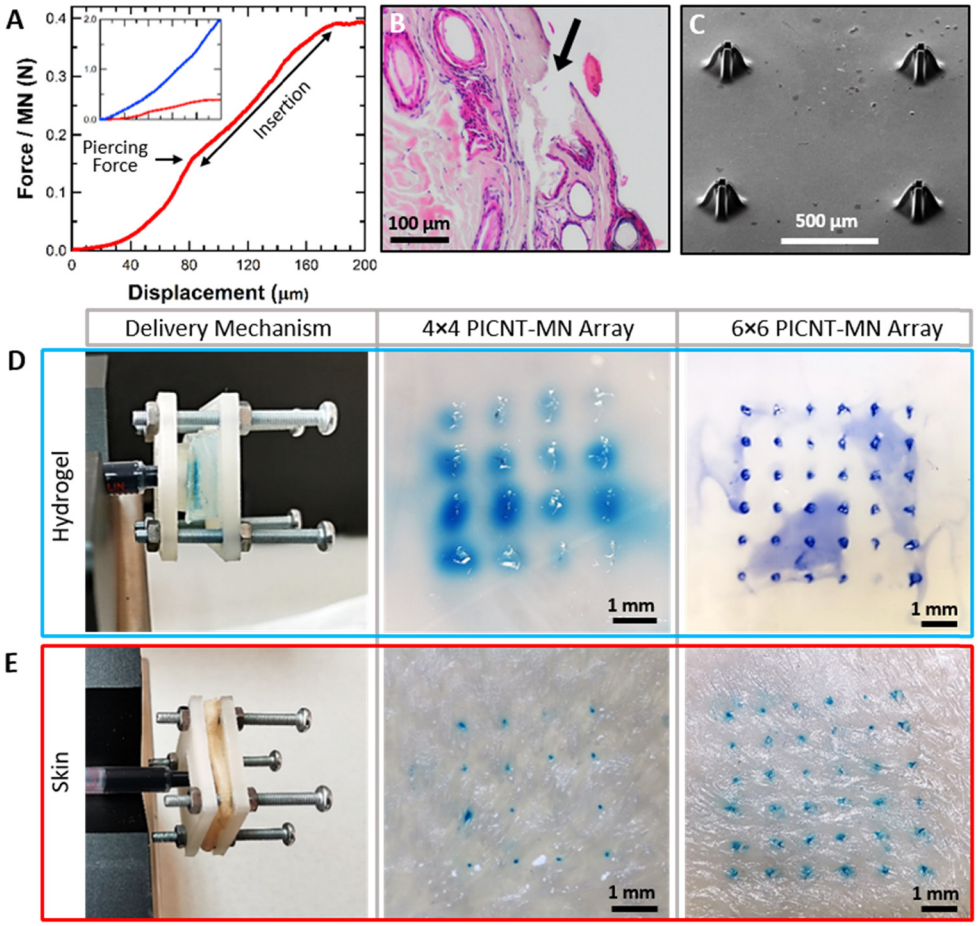


Fig. 6 (A) The force *versus* displacement curve measured during the tapered PICNT-MN array insertion into the skin. The inset is the comparison of the force *versus* displacement curves of the tapered (red) and the straight (blue) PICNT-MN arrays. (B) Histological image of the skin after the tapered PICNT-MN insertion. (C) SEM image of the tapered PICNT-MN array after repeated skin insertion tests. Methylene blue solution deliveries to (D) agarose hydrogel and (E) the skin with 4 × 4 and 6 × 6 PICNT-MN arrays.

Liquid delivery performance of the tapered and the straight PICNT-MN arrays were performed on agarose hydrogel and the rat skin (*in vitro*) as targeted media using methylene blue solution as a delivery. In order to obtain accurate measurements, the delivery mechanism shown in Fig. 6(D) and (E) was designed so that the PICNT-MNs are applied to the media with the same constant force throughout the liquid delivery (Movies S3 and S4, ESI†). Liquid deliveries were performed with increasing rate each time until there was methylene blue solution leakage out of media was observed. Thus, the maximum liquid delivery rates into the mediums with the PICNT-MN array without leakage are determined. This also prevented erroneously measuring the liquid that accidentally delivered outside as if it was delivered into the medium. After successful attempts with 4 × 4 and 6 × 6 PICNT-MN arrays, the deliveries of methylene blue solution into the hydrogel were viewed using an optical microscope (Fig. 6(D)). The maximum liquid delivery rate measured per the tapered PICNT-MN for the hydrogel was 3.75 μL $min^{-1}$. This equals the rate of 60 μL $min^{-1}$ for 4 × 4 PICNT-MN array and 240 μL $min^{-1}$ for a 8 × 8 PICNT-MN array. The images of the skins after methylene blue solution deliveries are given in Fig. 6(E).

The maximum liquid delivery rate reached per the tapered PICNT-MN for the skin was 0.31 μL $min^{-1}$ which is 12 times lower than the rate for the hydrogel due to the dense structure of the skin that resists liquid diffusion. The delivery rates for 4 × 4 and 8 × 8 PICNT-MN arrays into the skin were 5 μL $min^{-1}$ and 20 μL $min^{-1}$, respectively. For comparison, liquid deliveries were tested with the straight PICNT-MN array. The maximum liquid delivery rates per the straight PICNT-MN measured to the hydrogel and the skin were 3.15 μL $min^{-1}$ and 0.23 μL $min^{-1}$, respectively. Based on these delivery rates, the tapered PICNT-MNs provided 26% and 16% improvement in liquid deliveries to the skin and the hydrogel compared to the straight PICNT-MNs. The advantage of the tapered PICNT-MN in liquid delivery comes from its novel bi-level-tip. The liquid can get out of the MN and diffuse into the skin by passing between the spaced CNT micro-columns at the tip despite the skin clogging being mostly at the top of the MN tip.

The biocompatibility of the PICNT-MNs in terms of their possible cytotoxicity was also considered. The cytotoxicity of CNTs is an ongoing debate in the literature, especially non-functionalized CNTs exhibit great risk for cells.[54–57]

 

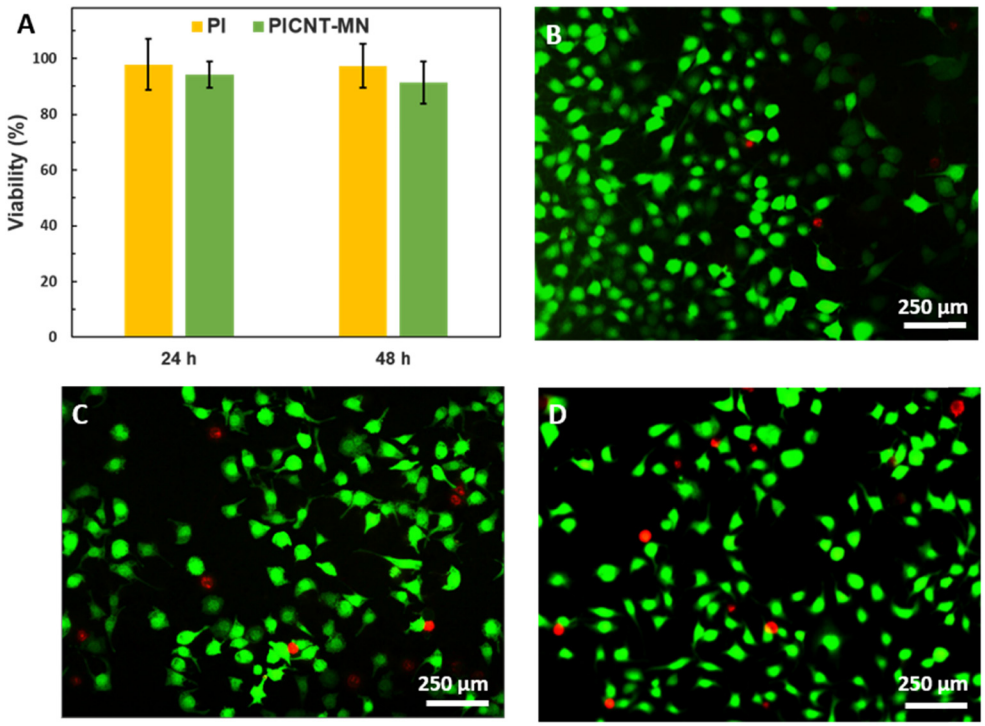


Fig. 7 (A) Indirect MTT results up to 24 h and 48 h. Results were normalized with respect to TCPS as control, assuming 100% viability. Fluorescence microscopy images of live/dead staining of (B) control, (C) PI and (D) PICNT-MN after 24 h. Calcein represents live cells (green) and EtBr represents dead cells (red).

However, the toxicity is significantly reduced after functionalization or coating with biocompatible materials.[58–61] On the other hand, PI is known as a biocompatible polymer and has been used in many biomedical applications.[62–64] We have investigated the cytotoxicity of PI and the PICNT-MNs on L929 mouse fibroblast cells. According to MTT results depicted in Fig. 7(A), both PI and the PICN-MNs showed quite biocompatible characteristics and no toxicity to the cells as cells maintained their viability as 97.39 ± 7.84 for PI and 91.36 ± 7.41 for PICNT-MNs at the end of 48 h. The cytotoxicity results were normalized to the control, here TCPS. In addition to the MTT results, the live/dead staining of both PI and the PICNT-MNs showed similar findings, as cells were healthy compared to the control. In this staining shown in Fig. 7(B)–(D), live cells might have been stained by calcein as calcein binds to cytoskeleton and dead cells might have been stained with Ethidium Bromide (EtBr) as EtBr is an intercalating agent for DNA. As a result of MTT and live/dead staining, it was concluded that the cytotoxicity of CNTs was suppressed with PI reinforcement.

## Conclusions

We have fabricated bi-level-tip tapered hollow MN arrays by utilizing the strain-engineered growth and capillary self-assembly of CNT microstructures together. The bottom-up fabrication enabled the creation of more scalable and functional MNs with fewer processing steps. The bottom-up approach provided more scalable MN fabrication with fewer processing steps, while the combination of the strain-engineered growth and capillary self-assembly enabled the creation of more functional MNs. The penetration and liquid delivery performance of the bi-level-tip tapered hollow MNs showed superior performance to the flat-tip straight hollow MNs due to its novel geometry. Cytotoxicity tests showed that PI reinforcement confers biocompatibility to CNT-MNs.

## Author contributions

N. U.: investigation, visualization, software; S. O.: formal analysis, methodology, supervision, validation, visualization; G. B. D.; formal analysis, methodology, supervision, validation, visualization; O. T. G.: conceptualization, data curation, formal analysis, funding acquisition, investigation, methodology, project administration, software, supervision, validation, visualization, writing-original draft, writing-review editing.

## Conflicts of interest

There are no conflicts to declare.

## Acknowledgements

This work was supported by the Scientific and Technological Research Council of Turkey (TÜBİTAK) under the Career Development Program (CAREER) (grant number 118M586). The authors thank Ms Sena Babadag and Mr Hakan Eskizengin

for Technical Assistance in Biological and Histological Assessments and Mr Abdullah Kafadenk for Technical Assistance in Cleanroom Processes.

## Notes and references

1 L. Wang and R. L. Coppel, *Expert Rev. Vaccines*, 2008, **7**, 729–738.
2 R. Singh, S. Singh and J. W. Lillard, *J. Pharm. Sci.*, 2008, **97**, 2497–2523.
3 J. G. Hilto, *J. Fam. Pract.*, 1995, **41**, 169–175.
4 Y. Nir, A. Paz, E. Sabo and I. Potasman, *Am. J. Trop. Med. Hyg.*, 2003, **68**, 341–344.
5 Y. C. Kim, J. H. Park and M. R. Prausnitz, *Adv. Drug Delivery Rev.*, 2012, **64**, 1547–1568.
6 S. Marshall, L. J. Sahm and A. C. Moore, *Hum. Vaccines Immunother.*, 2016, **12**, 2975–2983.
7 F. Wang, X. Zhang, G. Chen and Y. Zhao, *Res.*, 2020, 1–9.
8 M. I. Haq, E. Smith, D. N. John, M. Kalavala, C. Edwards, A. Anstey, A. Morrissey and J. C. Birchall, *Biomed. Microdevices*, 2009, **11**, 35–47.
9 H. R. Jeong, H. S. Lee, I. J. Choi and J. H. Park, *J. Drug Targeting*, 2017, **25**, 29–40.
10 J. J. Norman, J. M. Arya, M. A. McClain, P. M. Frew, M. I. Meltzer and M. R. Prausnitz, *Vaccine*, 2014, **32**, 1856–1862.
11 P. Van Damme, F. Oosterhuis-Kafeja, M. Van der Wielen, Y. Almagor, O. Sharon and Y. Levin, *Vaccine*, 2009, **27**, 454–459.
12 S. Moon, Y. Wang, C. Edens, J. R. Gentsch, M. R. Prausnitz and B. Jiang, *Vaccine*, 2013, **31**, 3396–3402.
13 X. Zhang, F. Wang, Y. Yu, G. Chen, L. Shang, L. Sun and Y. Zhao, *Sci. Bull.*, 2019, **64**, 1110–1117.
14 X. Zhang, G. Chen, F. Bian, L. Cai and Y. Zhao, *Adv. Mater.*, 2019, **31**, 1902825.
15 X. Zhang, L. Sun, Y. Wang, F. Bian, Y. Wang and Y. Zhao, *Proc. Natl. Acad. Sci. U. S. A.*, 2019, **116**, 20863–20868.
16 J. H. Park, S. O. Choi, S. Seo, Y. Bin Choy and M. R. Prausnitz, *Eur. J. Pharm. Biopharm.*, 2010, **76**, 282–289.
17 Y. C. Kim, F. S. Quan, D. G. Yoo, R. W. Compans, S. M. Kang and M. R. Prausnitz, *J. Infect. Dis.*, 2010, **201**, 190–198.
18 S. P. Sullivan, N. Murthy and M. R. Prausnitz, *Adv. Mater.*, 2008, **20**, 933–938.
19 F. J. Verbaan, S. M. Bal, D. J. van den Berg, J. A. Dijksman, M. van Hecke, H. Verpoorten, A. van den Berg, R. Luttge and J. A. Bouwstra, *J. Control. Release*, 2008, **128**, 80–88.
20 H. J. G. E. Gardeniers, R. Luttge, E. J. W. Berenschot, M. J. De Boer, S. Y. Yeshurun, M. Hefetz, R. Van't Oever and A. Van Den Berg, *J. Microelectromech. Syst.*, 2003, **12**, 855–862.
21 J. Ji, F. E. H. Tay, J. Miao and C. Iliescu, *J. Phys.: Conf. Ser.*, 2006, **34**, 186.
22 K. Kim, D. S. Park, H. M. Lu, W. Che, K. Kim, J. B. Lee and C. H. Ahn, *J. Micromech. Microeng.*, 2004, **14**, 597.
23 M. R. Maschmann, G. J. Ehlert, S. Tawfick, A. J. Hart and J. W. Baur, *Carbon N. Y.*, 2014, **66**, 377–386.
24 S. Ahmad, D. Copic, C. George and M. De Volder, *Adv. Mater.*, 2016, **28**, 6705–6710.
25 B. J. Lyon, A. I. Aria and M. Gharib, *Biomed. Microdevices*, 2014, **16**, 879–886.
26 N. Roxhed, T. C. Gasser, P. Griss, G. A. Holzapfel and G. Stemme, *J. Microelectromech. Syst.*, 2007, **16**, 1429–1440.
27 P. M. Wang, M. Cornwell, J. Hill and M. R. Prausnitz, *J. Invest. Dermatol.*, 2006, **126**, 1080–1087.
28 S. P. Davis, B. J. Landis, Z. H. Adams, M. G. Allen and M. R. Prausnitz, *J. Biomech.*, 2004, **37**, 1155–1163.
29 S. Tawfick, M. De Volder, D. Copic, S. J. Park, C. R. Oliver, E. S. Polsen, M. J. Roberts and A. J. Hart, *Adv. Mater.*, 2012, **24**, 1628–1674.
30 C. N. LaFratta, J. T. Fourkas, T. Baldacchini and R. A. Farrer, *Angew. Chem., Int. Ed.*, 2007, **46**, 6238–6258.
31 S. Reyntjens and R. Puers, *J. Micromech. Microeng.*, 2001, **11**, 287.
32 A. Del Campo and C. Greiner, *J. Micromech. Microeng.*, 2007, **17**, R81.
33 A. Bertsch, S. Jiguet and P. Renaud, *J. Micromech. Microeng.*, 2003, **14**, 197.
34 M. De Volder, S. Park, S. Tawfick and A. J. Hart, *Nat. Commun.*, 2014, **5**, 1–9.
35 M. De Volder and A. J. Hart, *Angew. Chem., Int. Ed.*, 2013, **52**, 2412–2425.
36 M. De Volder, S. H. Tawfick, S. J. Park, D. Copic, Z. Zhao, W. Lu and A. J. Hart, *Adv. Mater.*, 2010, **22**, 4384–4389.
37 E. J. García, A. J. Hart, B. L. Wardle and A. H. Slocum, *Nanotechnology*, 2007, **18**, 165602.
38 T. Wang, D. Jiang, S. Chen, K. Jeppson, L. Ye and J. Liu, *Mater. Lett.*, 2012, **78**, 184–187.
39 H. Ohno, D. Takagi, K. Yamada, S. Chiashi, A. Tokura and Y. Homma, *Jpn. J. Appl. Phys.*, 2008, **47**, 1956–1960.
40 X. Sun, K. Li, R. Wu, P. Wilhite, T. Saito, J. Gao and C. Y. Yang, *Nanotechnology*, 2009, **21**, 045201.
41 L. Delzeit, B. Chen, A. Cassell, R. Stevens, C. Nguyen and M. Meyyappan, *Chem. Phys. Lett.*, 2001, **348**, 368–374.
42 O. T. Gul, *Diamond Relat. Mater.*, 2021, **120**, 108637.
43 O. T. Gul, *Appl. Phys. A: Mater. Sci. Process.*, 2021, **127**, 1–11.
44 F. Bilimleri, E. Dergisi, A. Makalesi and O. T. Gül, *Erzincan Univ. J. Sci. Technol.*, 2020, **13**, 1354–1361.
45 Q. Zhao, M. B. Nardelli and J. Bernholc, *Phys. Rev. B: Condens. Matter Mater. Phys.*, 2002, **65**, 144105.
46 M. F. L. De Volder, S. H. Tawfick, R. H. Baughman and A. J. Hart, *Science*, 2013, **339**, 535–539.
47 B. I. Yakobson and P. Avouris, *Carbon Nanotubes*, 2001, 287–327.
48 H. L. Ma, Z. Jia, K. Tak Lau, X. Li, D. Hui and S. Qiang Shi, *Composites, Part B*, 2017, **110**, 396–401.
49 W. Yuan, J. Che and M. B. Chan-Park, *Chem. Mater.*, 2011, **23**, 4149–4157.
50 W. Chen, W. Chen, B. Zhang, S. Yang and C. Y. Liu, *Polymer*, 2017, **109**, 205–215.
51 R. W. Snyder, B. Thomson, B. Bartges, D. Czerniawski and P. C. Painter, *Macromolecules*, 2002, **22**, 4166–4172.
52 S. F. Lahiji, M. Dangol and H. Jung, *Sci. Rep.*, 2015, **5**, 1–7.



 

53 X. Jiang and P. B. Lillehoj, *Microsyst. Nanoeng.*, 2020, **6**, 1–11.
54 S. Pichardo, D. Gutiérrez-Praena, M. Puerto, E. Sánchez, A. Grilo, A. M. Cameán and Á. Jos, *Toxicol. In Vitro*, 2012, **26**, 672–677.
55 A. R. Murray, E. Kisin, S. S. Leonard, S. H. Young, C. Kommineni, V. E. Kagan, V. Castranova and A. A. Shvedova, *Toxicology*, 2009, **257**, 161–171.
56 Y. Liu, Y. Zhao, B. Sun and C. Chen, *Acc. Chem. Res.*, 2012, **46**, 702–713.
57 K. Donaldson, C. A. Poland, F. A. Murphy, M. MacFarlane, T. Chernova and A. Schinwald, *Adv. Drug Delivery Rev.*, 2013, **65**, 2078–2086.
58 A. Takagi, A. Hirose, M. Futakuchi, H. Tsuda and J. Kanno, *Cancer Sci.*, 2012, **103**, 1440–1444.
59 Z. Liu, S. Tabakman, K. Welsher and H. Dai, *Nano Res.*, 2009, **2**, 120.
60 M. Bottini, N. Rosato and N. Bottini, *Biomacromolecules*, 2011, **12**, 3381–3393.
61 S. T. Yang, J. Luo, Q. Zhou and H. Wang, *Theranostics*, 2012, **2**, 271.
62 C. P. Constantin, M. Aflori, R. F. Damian and R. D. Rusu, *Mater.*, 2019, **12**, 3166.
63 K. K. Lee, J. He, A. Singh, S. Massia, G. Ehteshami, B. Kim and G. Raupp, *J. Micromech. Microeng.*, 2003, **14**, 32.
64 K. Lee, A. Singh, J. He, S. Massia, B. Kim and G. Raupp, *Sens. Actuators, B*, 2004, **102**, 67–72.